

Stellar/Planetary Atmospheres

Part 14: Model Atmospheres

Peter Hauschildt
yeti@hs.uni-hamburg.de

Hamburger Sternwarte
Gojenbergsweg 112
21029 Hamburg

14. März 2018

Topics

- ▶ Basic Results from Model Atmospheres
 - ▶ T -structure of the Sun
 - ▶ T -structure of model atmospheres
 - ▶ T , P_{gas} , P_e relations
 - ▶ geometrical extension
 - ▶ effects of chemical abundances
 - ▶ T_{eff} effects
 - ▶ continua
 - ▶ behavior of spectral lines
- ▶ chemical analysis
- ▶ micro-turbulence
- ▶ graphs from Gray (1989) and France's PhD thesis

temperature structure: Sun

- ▶ observations of limb darkening (LD)
- ▶ plus Eddington-Barbier relation
- ▶ LD depends on $\lambda \rightarrow$
- ▶ S_λ varies with λ
- ▶ inferred T structures agree well with models
- ▶ inside the chromospheric T rise, of course!

LD in the Sun

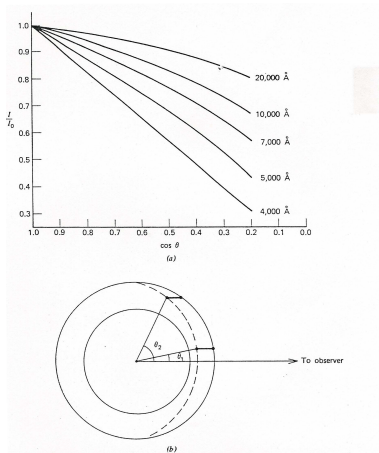


Fig. 9.2. (a) The limb-darkening observations of Pierce and Waddell (1961) are shown for several wavelengths. The 4000 Å curve is nearly linear. (b) A schematic illustration of the cause of limb darkening is shown. The top and bottom of the photosphere are indicated by the outer and inner circles. Penetration of our line of sight to unit optical depth, as indicated by the heavy line segments, corresponds to different depths in the photosphere depending on θ . The dashed curve indicates the surface of penetration to unit optical depth. Radiation seen at the disk position θ_2 is characteristic of the higher cooler layers than the radiation seen at the disk position θ_1 .

T structure: Sun

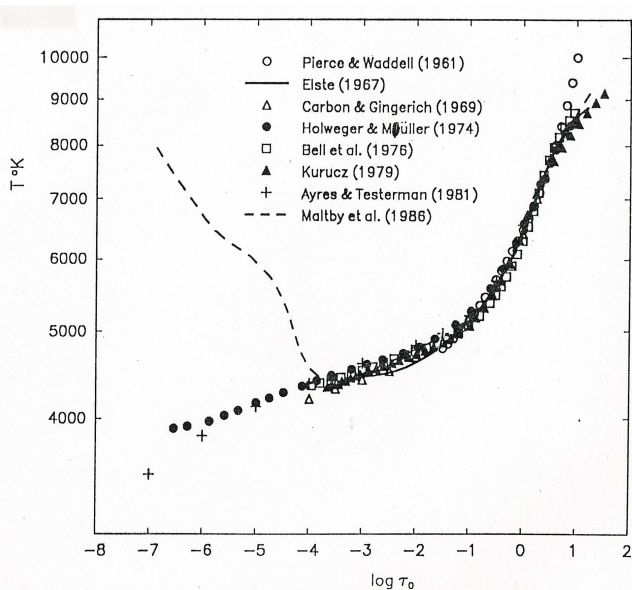


Fig. 9.4. Several solar temperature distributions are compared.

Model atmospheres

- ▶ typically computed in stages
 1. initial guess of structure (grey)
 2. continuum model
 3. line model
 4. NLTE model
- ▶ use scaled structures, too

line blanketing

- ▶ lines drastically change T structure!
- ▶ cool outer layers
- ▶ heat inner layers

line blanketing

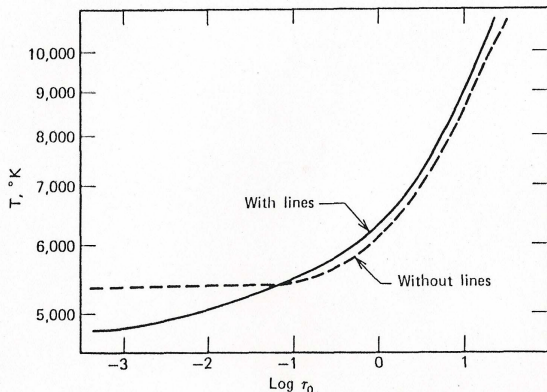


Fig. 9.5. Line blanketing raises the temperature deeper in the photosphere and lowers it in the outer regions. This model has $T_{\text{eff}} = 6500$ K, $\log g = 10^4$ cm/s², and solar abundances. Data are from Strom and Kurucz (1966).

convection

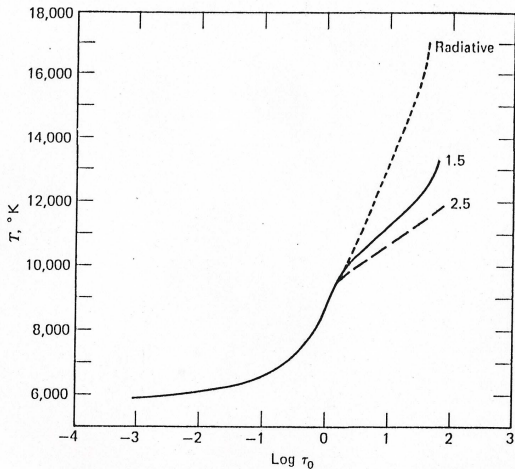


Fig. 9.6. Convection lowers the model's temperatures in the deep layers. The 'radiative' model has no convection. The others are labeled with the ratio of mixing length to pressure scale height. Little light escapes from the layers below $\text{log } \tau_0 \approx 0.5$. Data are from Carbon and Gingerich (1969).

convection

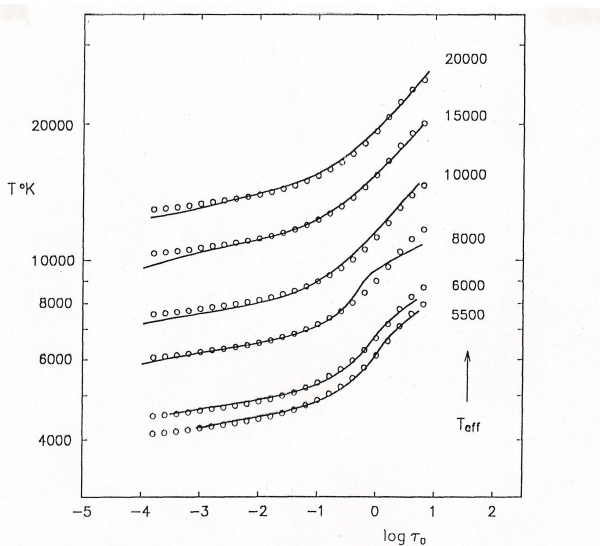


Fig. 9.7. Several temperature distributions (solid lines) derived by enforcing radiative equilibrium are compared to a model of the same grid having solar parameters, $T_{\text{eff}} = 5770$ K, $\log g = 4.44$ (dots). Data are from Kurucz (1979).

scaling relations

- ▶ scaled solar T structure quite useful

$$T(\tau) = S_0 T_{\odot}(\tau)$$

- ▶ P_{gas} does not scale as $T(\tau)$ (hydrostatic equation)
- ▶ can be approximated in the form

$$P_{\text{gas}} \propto g^p$$

- ▶ $p \approx 0.57 \dots 0.64$
- ▶ similar for P_e :

$$P_e \propto g^q$$

- ▶ $q \approx 0.45 \dots 0.3$

gravity effects

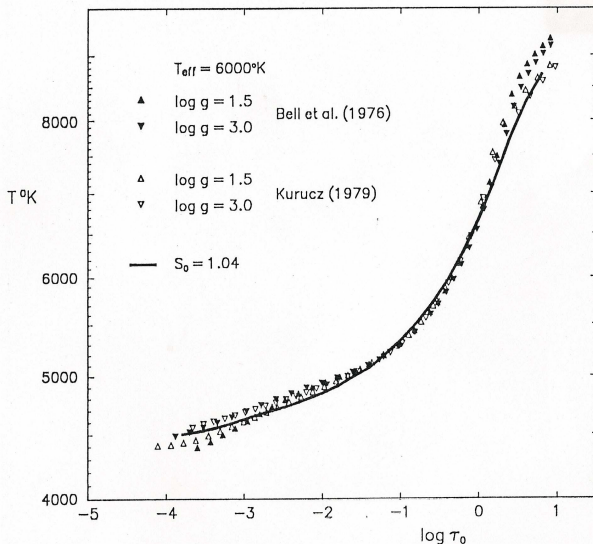


Fig. 9.8. Differences in $T(\tau_0)$ are shown for two surface gravities, as labeled. Lower surface gravity produces systematically lower temperatures in the upper layers. The scaled solar model is again shown for comparison (line).

T, P_{gas}, P_e relations

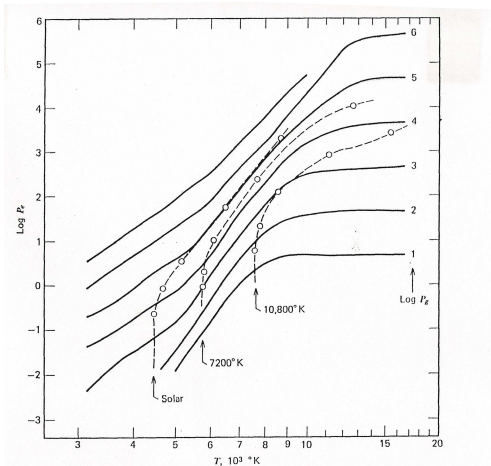


Fig. 9.10. The relation among P_g , P_e , and T is shown for material having normal solar chemical composition. The dashed lines show the points corresponding to three models. The surface gravity is 10^1 cm/s^2 for the two hotter models. Optical depth, τ_0 , in decades is denoted by the circles with the lowest ones having $\tau_0 = 10^{-3}$ and the highest ones 10. The cooler models show a nearly constant P_e over a significant range in depth.

geometrical depths of atmospheres

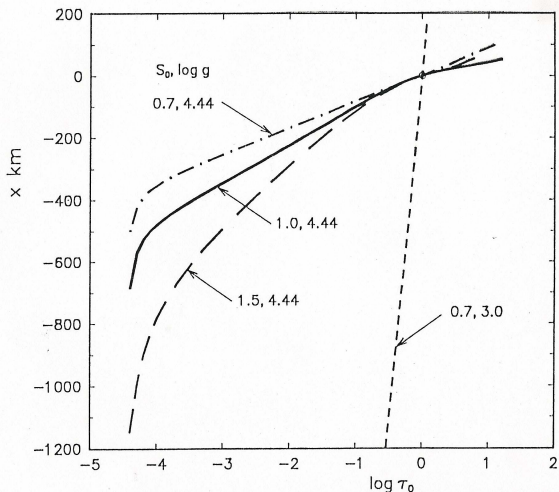


Fig. 9.11. Geometrical depth is nearly a linear function of $\log \tau_0$. The turn-down in the very shallow layers is a result of starting the integration and does not represent physical behavior. Each curve is labeled with its $S_0, \log g$ value. Notice the great sensitivity to gravity.

T, P_{gas} with convection

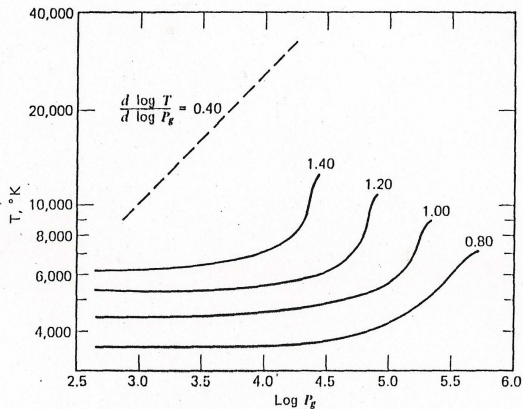


Fig. 9.15. The $\log T$ - $\log P_g$ plane is shown for four models, each labeled with its value of S_0 . The convective-limit temperature gradient is indicated.

T, P_{gas} with convection

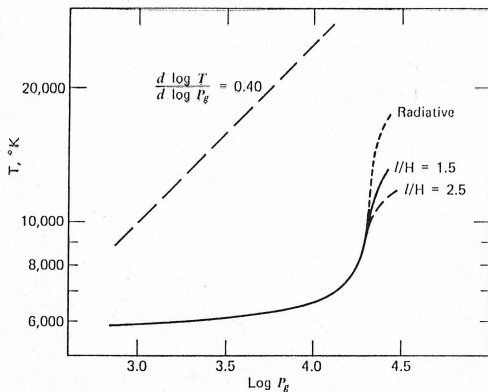


Fig. 9.16. The $\log T$ - $\log P_g$ plane is shown for the models of Fig. 9.6 in which we see the effects of the mixing-length parameter.

τ, P_{gas} relation

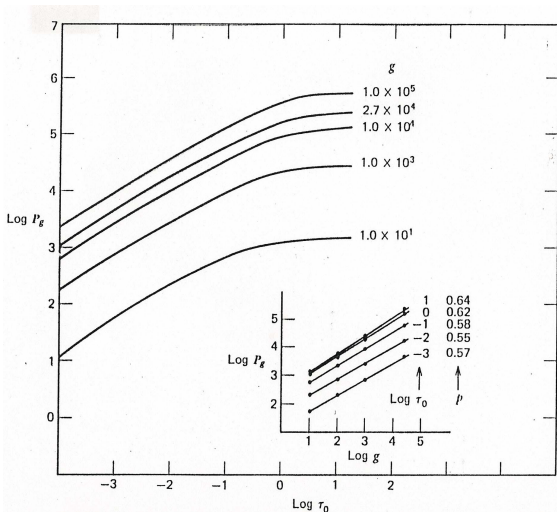


Fig. 9.17. The gas pressure shows a nearly linear relation with $\log \tau_0$, but levels off in the deep layers. Each line represents a model with the solar temperature and the surface gravity shown to the right of the curve. The inset shows that $\log P_g$ at any given depth varies linearly with $\log g$. The slope p is indicated.

τ, P_e relation

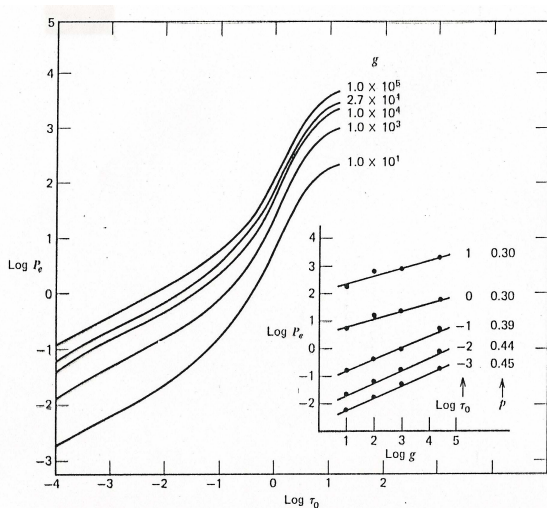


Fig. 9.18. The electron pressure shows a much larger change with depth than the gas pressure (Fig. 9.17). Each line represents a model with the solar temperature and the surface gravity shown next to the curve. The inset shows that $\log P_e$ at any given depth varies more-or-less linearly with $\log g$. The slope p is indicated.

effects of chemical composition

- ▶ solar type stars:
 - ▶ most electrons provided by metals (Na!)
 - ▶ → significant effect of metallicity
- ▶ hotter stars: H is most important electron donor
 - ▶ → abundance effects smaller
- ▶ cooler stars:
 - ▶ increasing metallicity increases number of free electrons
 - ▶ opacity increases
 - ▶ → decreasing P_{gas} at given τ

effects of metallicity

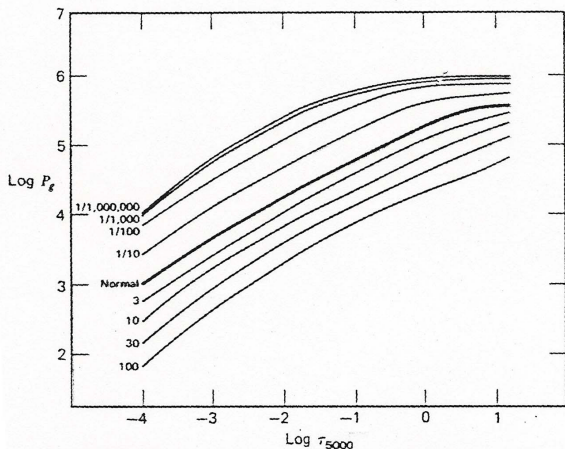


Fig. 9.19. An increase in the metal abundance (factor shown) leads to a decrease in gas pressure at each optical depth for these cool models. This is a result of the increase in opacity caused by the increase in electron donors and the subsequent reduction in the depth of penetration of the line of sight.

effects of metallicity

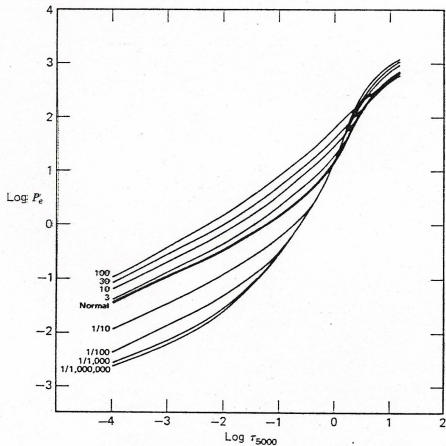


Fig. 9.20. An increase in metal abundance (factor shown) leads to an increase in the electron pressure at most depths in these cool models. The interesting cross-over in the deeper layers arises when the metals are underabundant, resulting in fewer electron donors and lower opacity allowing us to see to the deeper layers where hydrogen becomes a significant contributor of electrons.

effects of T_{eff}

- ▶ increase $T_{\text{eff}} \rightarrow$
- ▶ opacity increases \rightarrow
- ▶ \rightarrow decreasing P_{gas} at given τ
- ▶ changes as H ionizes
- ▶ P_e increases with T_{eff} due to increasing ionization

effects of T_{eff}

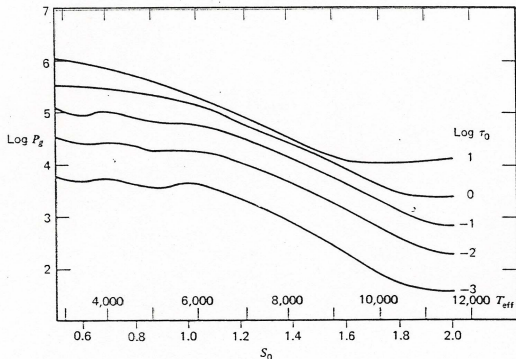


Fig. 9.21. The gas pressure decreases at each optical depth as the model temperature rises.

effects of T_{eff}

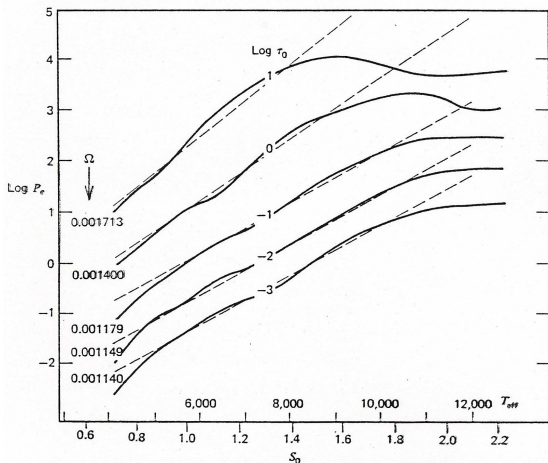


Fig. 9.22. The electron pressure increases with increasing model temperature until a leveling off occurs where hydrogen takes over as the electron donor. In the domain of cooler temperatures, $\log P_e$ varies approximately linearly with temperature. The Ω of eq. (9.18) is shown on the left.

continua from model atmospheres

- ▶ significant deviations from BBs!
- ▶ examples use scaled solar T structures
- ▶ Balmer jump strongly T_{eff} dependent
- ▶ less g dependent
- ▶ low $T_{\text{eff}} \rightarrow \text{H}^-$ dominates
- ▶ can be used to fit to observed 'continua' (hotter stars only!)
- ▶ use T_{eff} dependence of Paschen continuum
- ▶ use g dependence of Balmer jump for given T_{eff}
- ▶ also: use synthetic colors and BCs for quick and dirty parameter estimates

stellar continua

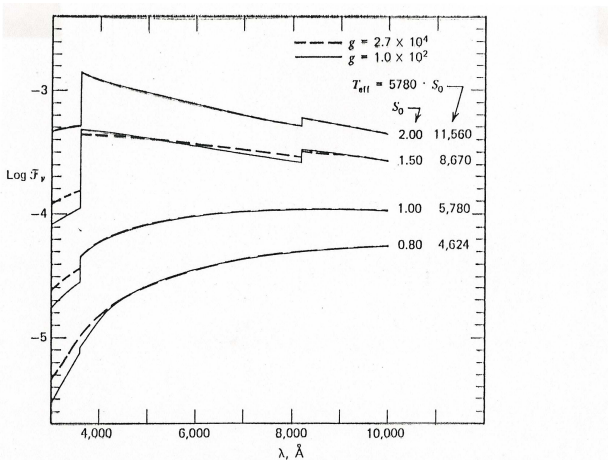


Fig. 10.8. Model-photosphere continua are shown for several scaled solar models as labeled. They are plotted on an absolute flux scale, and so both the slope and height of the graph changes with temperature. The gravity dependence (solid versus dashed lines) is relatively weak.

stellar continua

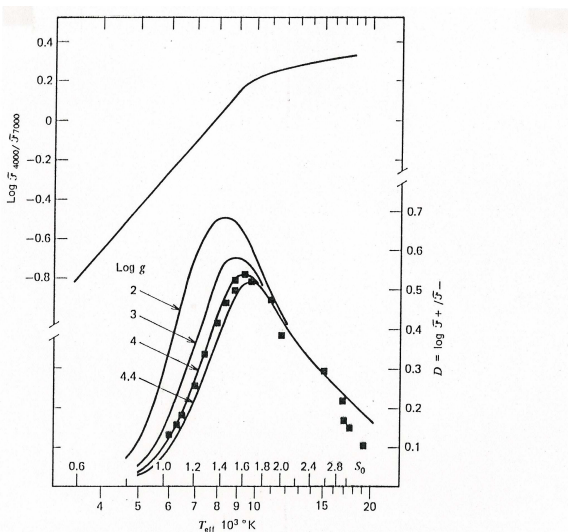


Fig. 10.9. The upper curve shows the smooth variation of the Paschen continuum with temperature. The lower curves show the temperature variation of the Balmer jump for several values of surface gravity. Smaller gravity enhances the Balmer jump. The models use a scaled solar $T(\tau_0)$. The squares show the observations tabulated by Barbier (1958).

stellar continua

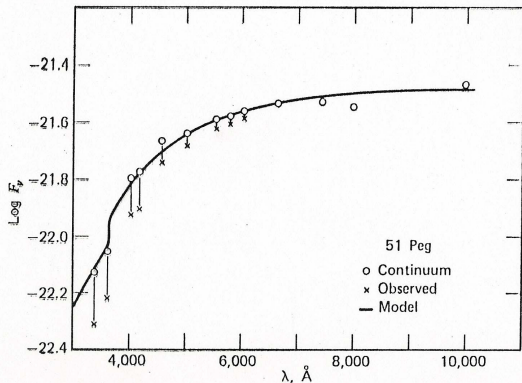


Fig. 10.13. The observed energy distribution of 51 Peg is shown by the \times s. Correction for line absorption gives the continuum (circles), which are then compared to a scaled model having $S_0 = 0.98$ (line).

stellar continua

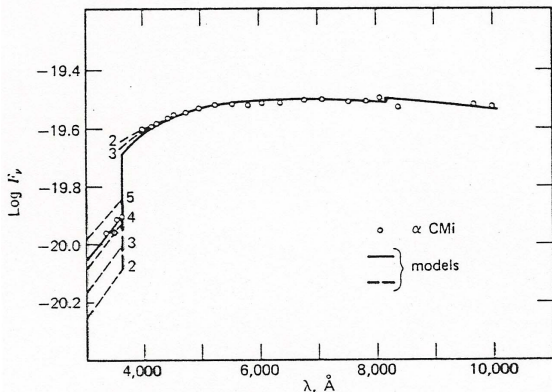
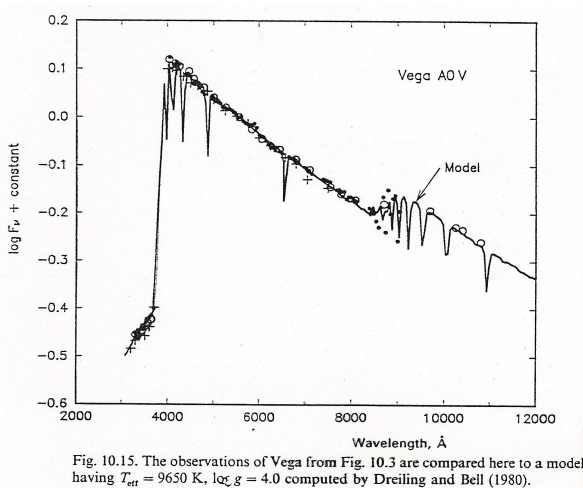


Fig. 10.14. These observations of Procyon (F5 IV–V) by Bessell (1967) are compared to a scaled solar model having $S_0 = 1.20$ and the values of $\log g$ shown. The model with $g = 2.7 \times 10^4 \text{ cm/s}^2$ is shown by the solid line.

stellar continua



bolometric corrections

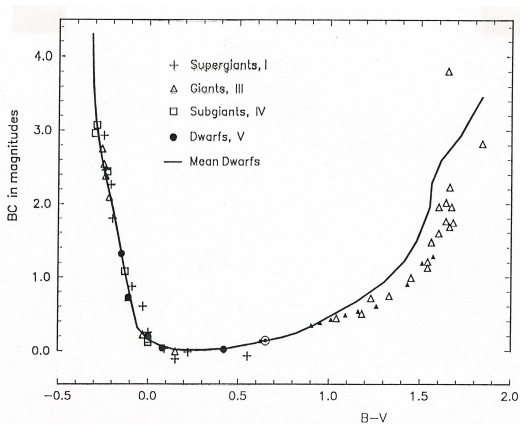


Fig. 10.16. Bolometric corrections are shown as a function of $B-V$ color index. The solid line is the mean relation for dwarfs Hayes (1978), and the small filled triangles is the relation given by Popper (1980). Other symbols are measurements for individual stars, and come from Code *et al.* (1976) and Hayes (1978).

behavior of spectral lines

- ▶ line source function

$$S_\nu = \frac{\bar{J} + \epsilon(\tau)B_\nu}{1 + \epsilon(\tau)}$$

- ▶ lines profile essentially maps $S_\nu(\tau)$
- ▶ \rightarrow use this to estimate $T(\tau)$ from lines

lines

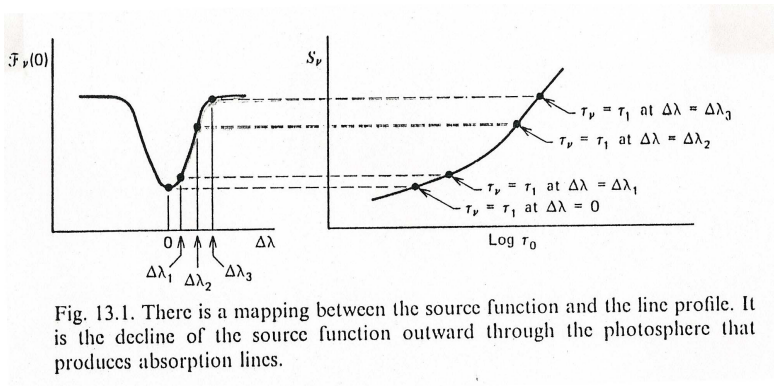


Fig. 13.1. There is a mapping between the source function and the line profile. It is the decline of the source function outward through the photosphere that produces absorption lines.

contribution function

- ▶ LTE line profile:

$$\begin{aligned}F_\nu &= 2\pi \int_0^\infty B_\nu(\tau_\nu) E_2(\tau_\nu) d\tau_\nu \\&= 2\pi \int_0^\infty B_\nu(\tau_\nu) E_2(\tau_\nu) \frac{d\tau_\nu}{d\tau_{\text{std}}} d\tau_{\text{std}} \\&= 2\pi \int_0^\infty \left[B_\nu(\tau_\nu) E_2(\tau_\nu) \frac{\chi_l + \chi_c}{\chi_{\text{std}}} \tau_{\text{std}} \right] \frac{d \log \tau_{\text{std}}}{\log e}\end{aligned}$$

- ▶ expression in $[\]$ → contribution function
- ▶ approximately measures contribution of each layer to line emission

lines

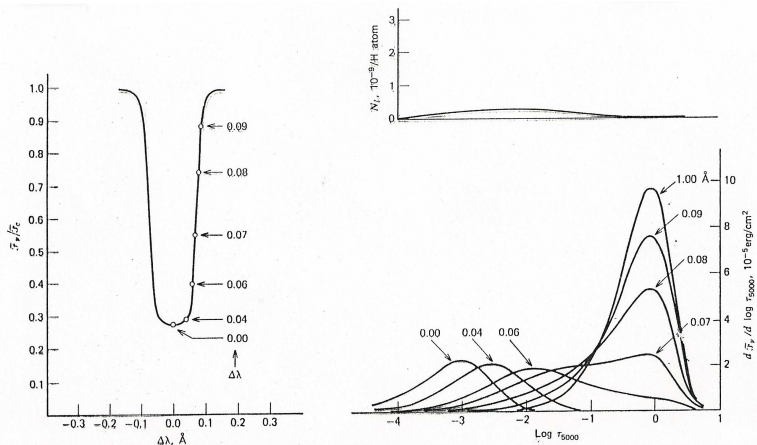


Fig. 13.2. The contribution functions for residual flux are shown for iron I $\lambda 6065$ with χ taken to be zero; the model has $S_0 = 1.02$ and $g = 10^4 \text{ cm/s}^2$. The line profile is shown at the left; the number of line absorbers and the integrands of eq. (13.15) on the right. Each labeled point on the profile has a corresponding contribution function on the right, as labeled.

lines

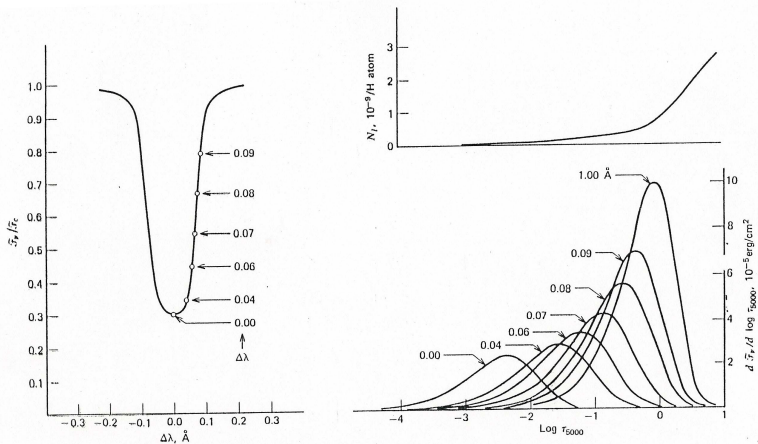


Fig. 13.3. This diagram is the same as Fig. 13.2 except for having $\chi = 5$ eV.

lines

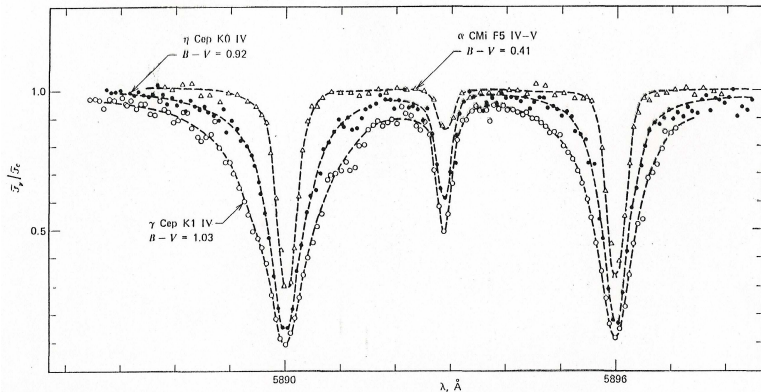


Fig. 13.7. The sodium D lines weaken with increasing temperature. These measurements were made with a spectral-line scanner having a resolution $\approx 0.27 \text{ \AA}$. The curves are drawn in by hand to guide the eye.

lines

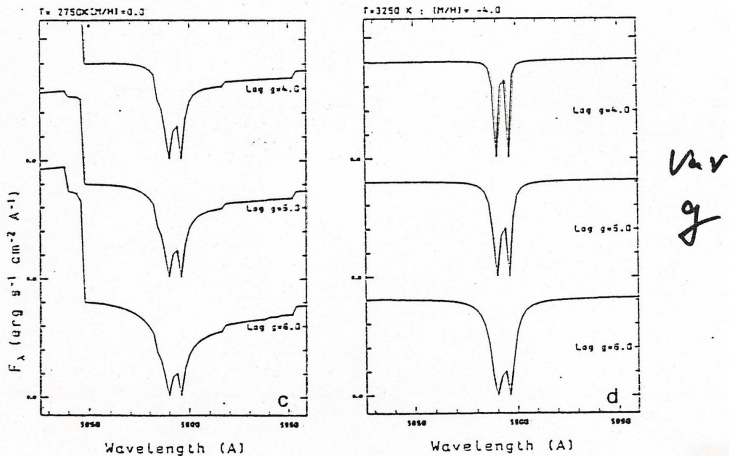
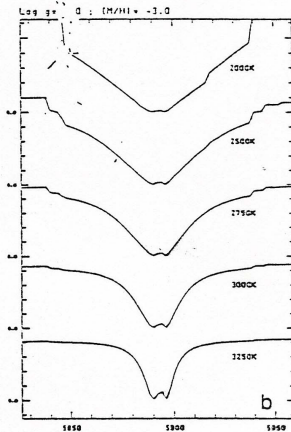
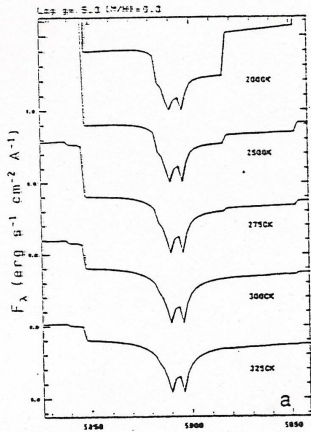


Figure 18: Variation of the profile of the NaI D resonance lines with a), b) the effective temperature T_{eff} at fixed gravity and metallicity, and c), d) the gravity ($\text{log } g$) at fixed T_{eff} and metallicity. The fixed parameters are indicated on the upper left corner of each figure. The jump at 5850\AA is due to the γ' band of TiO.

lines



var
Teff

lines

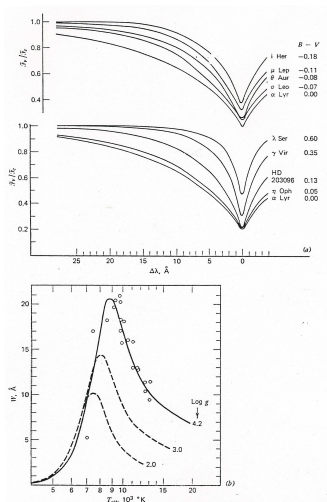


Fig. 13.8. (a) Observations of H α are shown. On top are profiles for stars hotter than $T_{\text{eff}} \approx 9000$ K, where the lines are strongest. Those cooler than this value are shown on the bottom. Adapted from Gray and Evans (1973). (b) The change in equivalent width of H α is shown as a function of temperature. Model calculations of Carbon and Gingerich (1969) are shown by the solid lines (log g indicated). The circles are measured values based on the data of Gray and Evans (1973).

lines

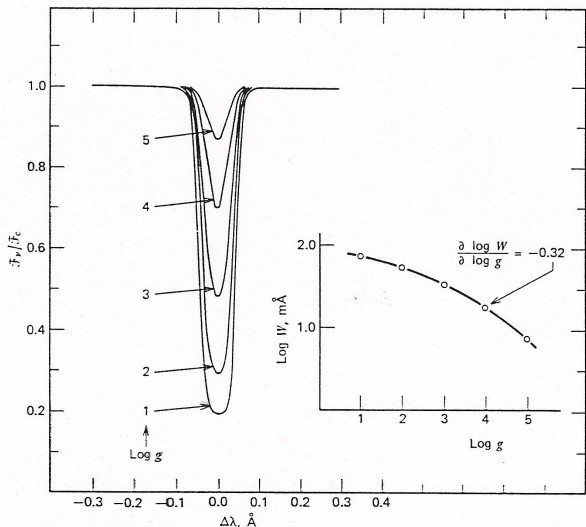


Fig. 13.9. Calculated profiles of iron II $\lambda 4508$ are shown for several values of surface gravity (cm/s^2). The inset graph shows the change in equivalent width. The model has $S_0 = 1.00$ and $A(\text{He}) = 0.1$.

lines

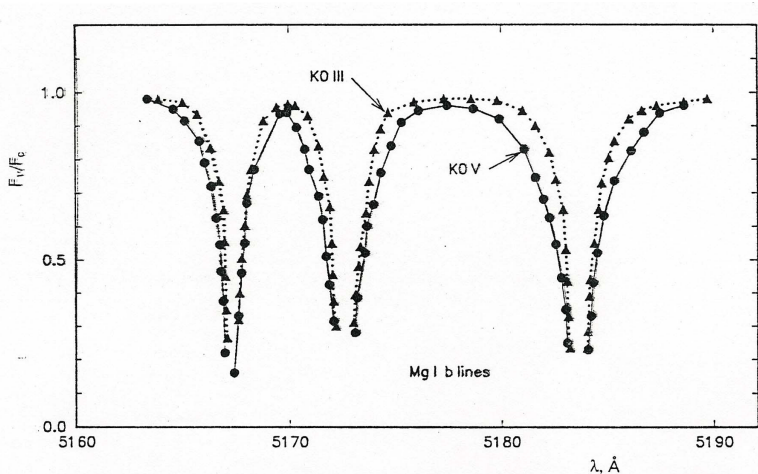
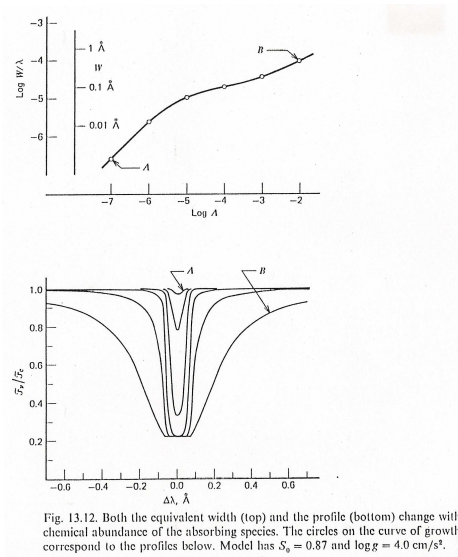


Fig. 13.10. The pressure dependence of the magnesium I b lines can be seen in this comparison. The dwarf is σ Dra; the giant HR 7042. (Adapted from Cayrel de Strobel (1969) with permission from the MIT Press.)

curve of growth



curve of growth

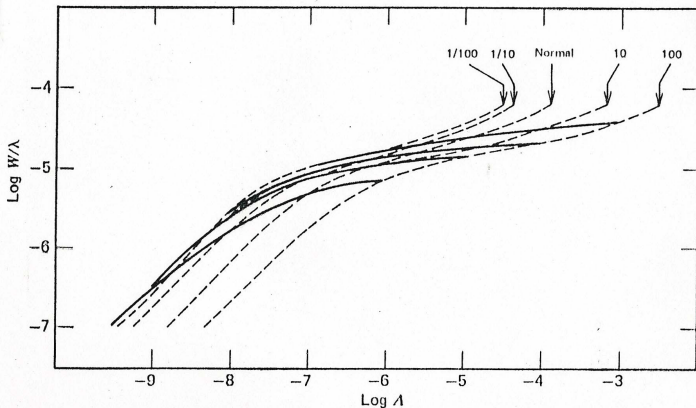


Fig. 13.13. The actual change in equivalent width of pressure-sensitive lines, like this iron II line, depend on the chemical composition of the model. Curves of growth are shown for five model abundances (-----), each labeled with its enhancement factor (relative to the solar composition). The heavy lines show the change when the model's composition changes in step with the specific chemical being studied.

line shapes

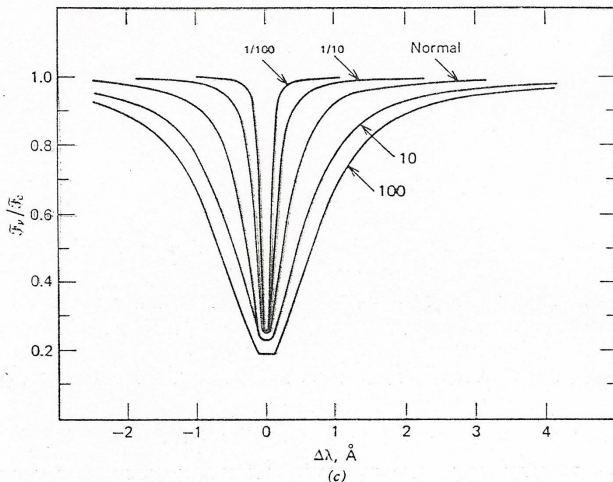
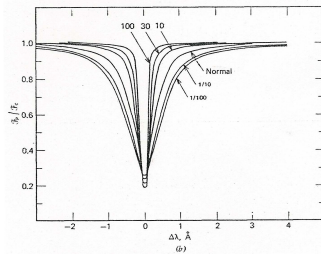
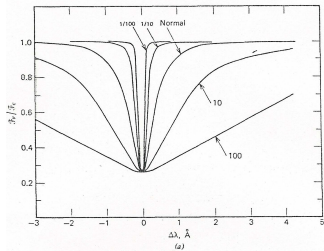


Fig. 13.14. The abundance behavior of the sodium D lines are shown for three cases: (a) has constant model abundances, sodium abundance changes as labeled, (b) has a constant sodium abundance, model abundances changes as labeled, and (c) shows the change when both model and sodium abundance are varied together as labeled.

line shapes



line profile comparisons

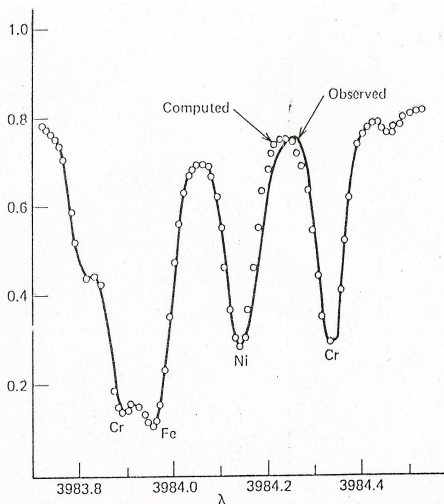


Fig. 14.9. A portion of the solar spectrum is compared here with a synthesis. (Adapted from Ross and Aller (1968) with permission of the *Astrophysical Journal*, copyright 1968 by the University of Chicago.)

line profile comparisons

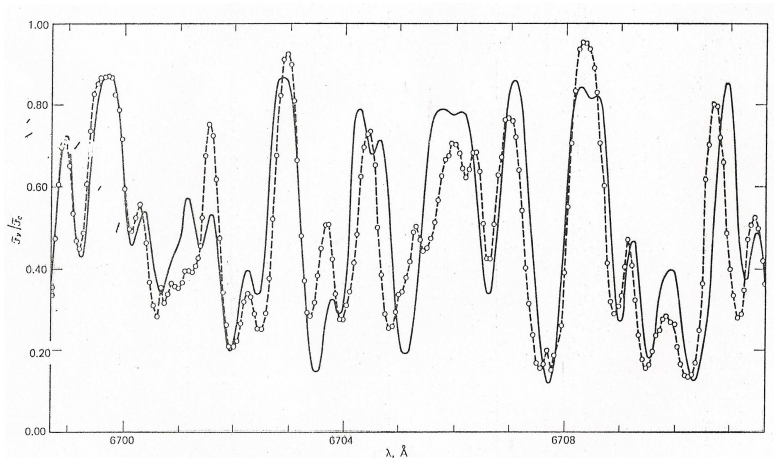


Fig. 14.10. The observed spectrum of HR 9004 = TX Psc (—), a cool carbon giant, is compared to the synthesized spectrum (---). (Courtesy of H.R. Johnson.)

low resolution comparison

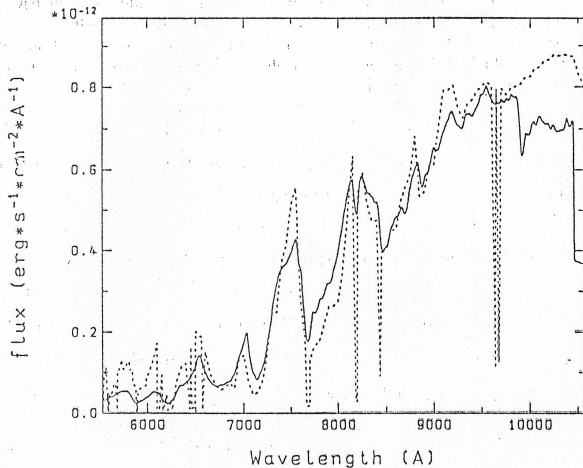


Figure 30: Low resolution spectrum of Gliese 866 (—) and the combined synthetic spectra of a 3000K dwarf and a 2500K dwarf with $\log g = 5.0$ and solar metallicity (···). Synthetic and observed spectra are matched at 8500Å. The band head of FeH at 9800Å is not reproduced due to the lack of molecular data.

higher resolution comparison

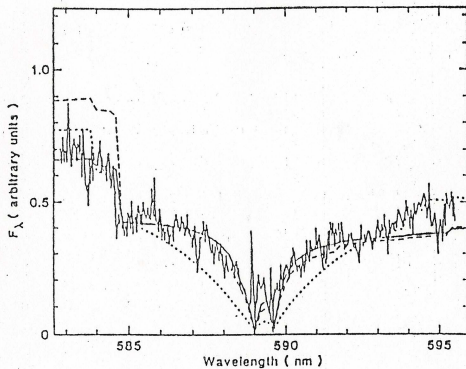


Figure 29: Fit to the observed NaD profile. Synthetic and observed profiles are matched at 5850\AA . Three synthetic profiles are presented: profile of a 3000 K dwarf with $\log g = 5.0$, solar abundances (—); profile of a 2750 K dwarf, with $\log g = 5.0$, solar abundances (- - -); profile of a dwarf with 3000 K, $\log g = 5.0$, reduced metallicity $Z = -1.0$ (···). Much of the apparent noise is due to TiO bands, metal absorption lines or to terrestrial features.

chemical analysis

- ▶ typically uses curve of growth methods
- ▶ problem: divide between the various effects involved in line formation
- ▶ T_{eff} , g , convection, abundances, blending, turbulence, rotation . . .
- ▶ CoG methods need accurate equivalent widths measurements
- ▶ very difficult for heavy blending (UV)
- ▶ accurate atomic data are also needed
- ▶ differential analyses circumvent the last problem!
- ▶ this delivers relative abundances

chemical analyses

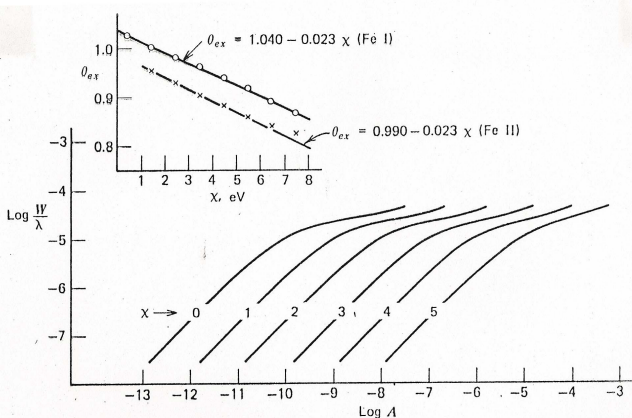


Fig. 14.1. Curves of growth shift to the right as the excitation potential is increased. These curves are computed for iron I in a solar-temperature model with a surface gravity to 10^4 cm/s^2 . The inset graph shows the shift between adjacent curves, $\Delta \log A$, divided by their mean χ as a function of χ . The relation for iron II is also shown.

chemical analyses

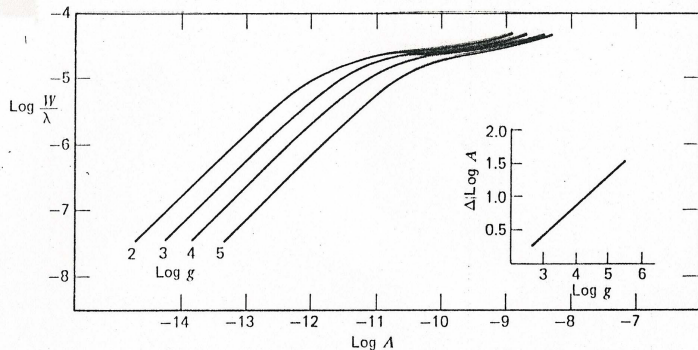


Fig. 14.2. Curves of growth for iron II are surface-gravity dependent in cool stars.

chemical analyses

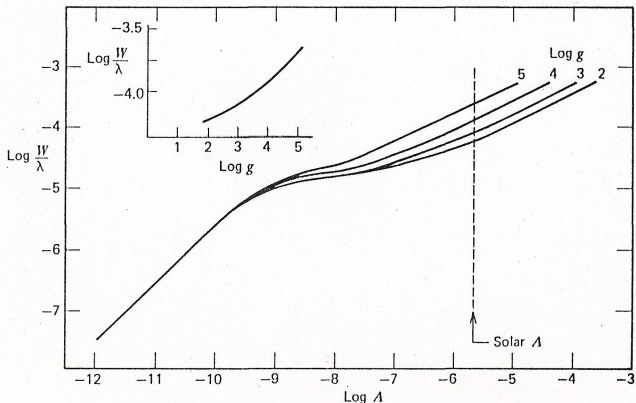


Fig. 14.3. The sodium D_2 line grows differently for difference surface gravity because of the gravity dependence of its damping constant. The models have $S_0 = 1.00$. The inset graph shows the cut through the curves at the solar sodium abundance.

chemical analyses

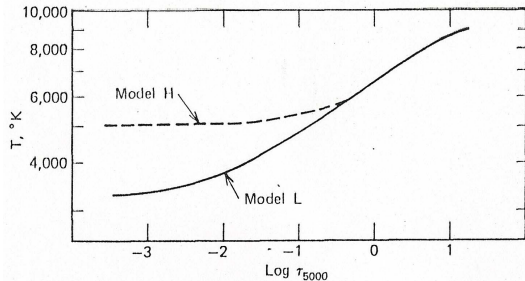


Fig. 14.5. These hypothetical temperature distributions produce very different behavior in lines formed in the upper photosphere as shown in the next figure. (H = higher temperatures; L = lower.)

chemical analyses

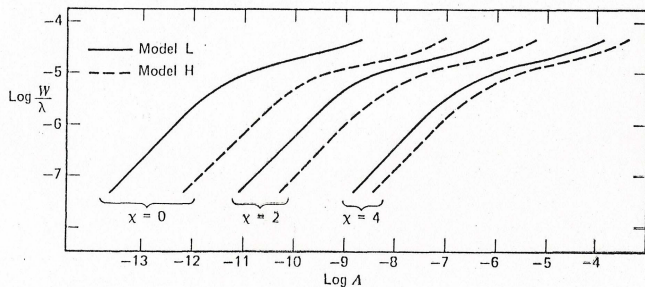


Fig. 14.6. These curves of growth correspond to the two temperature distributions shown in the previous figure. Large displacements are obvious, but there are also small differences in the saturation levels of the curves that result in different deduced values for the microturbulence dispersion.

micro-turbulence

- ▶ comparison observed-theoretical line profiles
- ▶ → observed lines often broader than computed lines
- ▶ stars with higher L often have broader lines
- ▶ → turbulence in stellar atmospheres
- ▶ isotropic micro-turbulence → small scales
- ▶ large scale macro-turbulence

micro-turbulence

- ▶ isotropic micro-turbulence →
- ▶ introduce micro-turbulent velocity ξ
- ▶ Doppler width →

$$\Delta\lambda_D = \frac{\lambda_0}{c} \sqrt{\frac{2kT}{m} + \xi^2}$$

- ▶ changes width and depth of a line →
- ▶ changes CoG
- ▶ ξ has to be determined line all other parameters
- ▶ different lines of the same element must give the same abundances

micro-turbulence

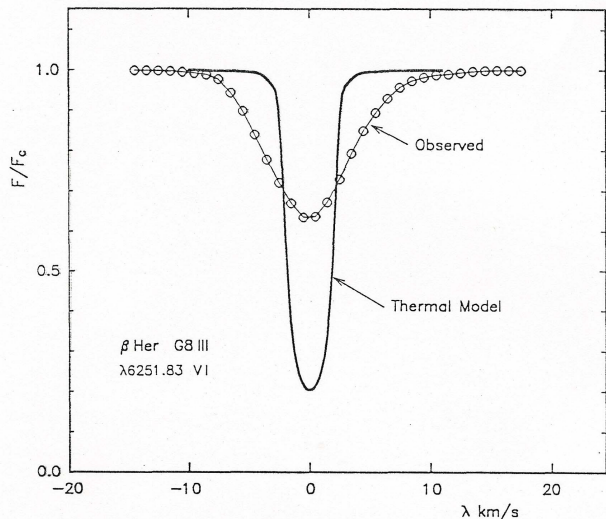


Fig. 18.1. The thermal profile computed from a model photosphere does not look much like the observed one. (From Gray (1988).)

micro-turbulence

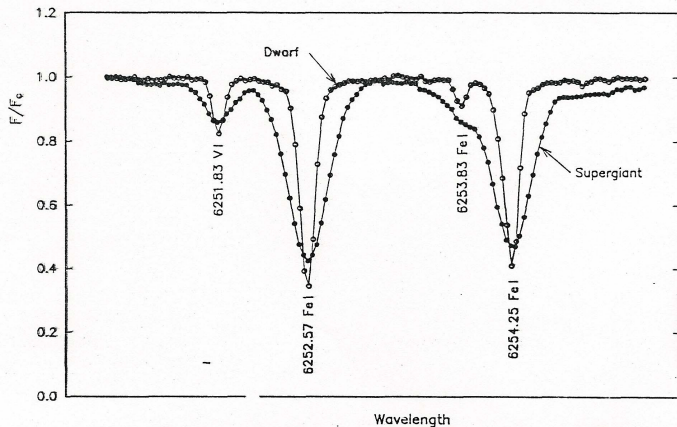


Fig. 18.2. Nonthermal broadening increases with luminosity. Notice how the cores of the lines are less deep for the supergiant.

micro-turbulence

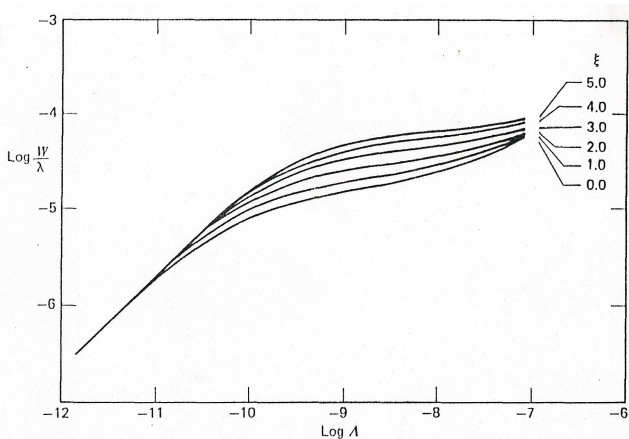


Fig. 14.4. Microturbulence delays saturation by spreading the absorption over a wider spectral band. Values of velocity dispersion, ξ , for an assumed Gaussian velocity distribution are in kilometers per second.